



Contents lists available at ScienceDirect

Journal of Aerosol Science

journal homepage: www.elsevier.com/locate/jaerosci

Application of the characteristics-based sectional method to spatially varying aerosol formation and transport



E.M.A. Frederix^{a,*}, A.K. Kuczaj^{d,a}, M. Nordlund^d, A.E.P. Veldman^{c,a}, B.J. Geurts^{a,b}

^a Multiscale Modeling and Simulation, Faculty EEMCS, University of Twente, P.O. Box 217, 7500 AE Enschede, The Netherlands

^b Anisotropic Turbulence, Fluid Dynamics Laboratory, Faculty of Applied Physics, Eindhoven University of Technology, P.O. Box 513, 5600 MB Eindhoven, The Netherlands

^c Institute of Mathematics and Computing Science, University of Groningen, P.O. Box 407, 9700 AK Groningen, The Netherlands

^d Philip Morris International R & D, Philip Morris Products S.A., Quai Jeanrenaud 5, 2000 Neuchatel, Switzerland

ARTICLE INFO

Keywords:

Aerosol
Eulerian
Multi-phase
Characteristics
Droplet size distribution
Sectional
PISO
Coagulation
Condensation
Nucleation

ABSTRACT

The characteristics-based sectional method (CBSM) offers an Eulerian description of an internally mixed aerosol. It was shown to be robust and capable of exact preservation of lower order moments, allowing for highly skewed sectional droplet size distributions. In this paper we apply CBSM to a spatially varying flow, by incorporating the fractional step method. In this way an accurate time integration of the spatial terms in the transport equations for the velocity, mass fractions and sectional droplet concentrations is achieved. Integrating CBSM into the compressible PISO (Pressure-Implicit with Splitting of Operators) algorithm allows for phase change and corresponding changes in pressure. We apply CBSM to a lid-driven cavity flow. First, the steady state isothermal flow solution is validated against published data. Next, by releasing a saturated vapor into the cavity while cooling the walls, we simulate the formation of aerosol. The accuracy of the solution is studied, as well as the performance of the CBSM scheme in the spatially varying context. The solution of the velocity is shown to be accurate, even at CFL (Courant–Friedrichs–Lewy) numbers of unity. The feasibility of the developed method is demonstrated in a 3D complex geometry studying the aerosol generation via nucleation of hot vapors cooled by a dilution stream of cold air in a double-mixing tee system. The sectional approach delivers detailed information about the aerosol formation and size distribution of the droplets in the domain.

1. Introduction

In aerosol science a common way of mathematically describing the dispersed phase is by adopting a continuous size distribution, expressing the concentration of droplets with a certain size or composition in space and time. Such a description, without the expensive necessity of tracking each individual particle, allows to investigate size-dependent aerosol processes, such as filtration, deposition, drift and light refraction. A popular method of finding a numerical approximation to the size distribution is the sectional approach (Gelbard, Tambour, & Seinfeld, 1980), in which the size domain is split up into discrete sections, each containing droplets within a pre-defined size range. The evolution of the size distribution is then governed by a manageable number of balance equations for each section.

In Frederix, Stanic, Kuczaj, Nordlund, and Geurts, (2016) CBSM was proposed and illustrated in spatially homogeneous

* Corresponding author.

E-mail address: e.m.a.frederix@utwente.nl (E.M.A. Frederix).

Nomenclature			
Δt	time step size	J_{coa}	coagulation rate
Δx	cell size	J_{nuc}	nucleation rate
β	coagulation kernel	k	iteration index superscript
δ	Dirac delta function	k_B	Boltzmann constant
κ	mixture thermal conductivity	L	size of the cavity
κ_l^*	pure constituent liquid thermal conductivity	M	number of species
κ_v^*	pure constituent vapor thermal conductivity	m	time level index superscript
μ	mixture viscosity	N	droplet number concentration
∇	nabla operator	n	droplet size distribution function
∂_t	partial time derivative	N_c	number of computational volumes
∂_z	partial droplet size derivative	N_P	number of iterations
ψ^*	vapor compressibility ratio	\mathbf{p}	discrete pressure vector
ρ	mixture mass density	P	number of sections
ρ^*	pure constituent liquid mass density	p	pressure
σ	droplet surface tension	Q	molar mean molecular weight
σ_g	geometric standard deviation	Re	Reynolds number
τ	rate of strain tensor	r_P	PISO pressure equation residual
θ	weight for θ -scheme	S	vapor-to-liquid mass transfer rate
\mathbf{A}	discrete pressure equation coefficient matrix	S_{cond}	vapor-to-liquid condensation mass transfer rate
\mathbf{b}	discrete pressure equation source vector	S_{nuc}	vapor-to-liquid nucleation mass transfer rate
CFL	Courant–Friedrichs–Lewy number	S^s	vapor saturation ratio
CMD	count median diameter	T	temperature
c_P	mixture heat capacity at constant pressure	t	time
D	pipe diameter	\mathbf{u}	mixture velocity
d	droplet diameter	U	velocity magnitude
D^*	diffusion coefficient	\mathbf{u}_c	species-independent diffusive correction velocity
d_c	count mean diameter	\mathbf{v}	diffusive vapor velocity
d_g	geometric mean diameter	V_m	molecular volume
d_{HC}	Hatch–Choate theoretical count mean diameter	\mathbf{x}	position vector
D_t	material time derivative	X	vapor mole fraction
E	Kelvin effect factor	Y	vapor mass fraction
e	convergence measure	y	sectional interface droplet mass
\mathbf{I}	identity tensor	Y^s	vapor equilibrium mass fraction
I	size dependent condensation rate	Z	liquid mass fraction
i	section index subscript	z	droplet mass
j	species index subscript	z_{nuc}	critical cluster size of nucleation

conditions of aerosol formation. The current paper extends this development and presents the corresponding method with which aerosol dynamics can be simulated in heterogeneous situations. This completes the necessary step toward a method that can be applied to realistic conditions of multiphase flow and phase changes. Such application is shown for aerosol formation in a 2D cavity and in a 3D double-mixing tee configuration.

The CBSM uses the condensational characteristics in the size domain to solve for nucleation and subsequent condensational growth of droplets. CBSM is based on the sectional formulation of Kumar and Ramkrishna (1996), in which each section contains a pre-specified representative size around which droplets are ‘sampled’. By distributing nucleated, grown or coagulated droplets over adjacent sections, one can analytically preserve a pre-selected number of moments of the size distribution. This is essential to conserve number and mass density, or other moments of the distribution. A second advantage which was introduced by CBSM is that, by using an analytic solution for condensational growth through tracking the characteristics of condensation, a robust algorithm is formulated not suffering from a severe time step restriction. Third, CBSM was shown to work on a highly skewed distribution of sections, e.g., a logarithmic distribution, which allows to span many orders of magnitude in the size domain at acceptable costs. To capture nucleation accurately, this was shown to be essential. Finally, through exact moment preservation CBSM may be constructed such that non-negativity of the size distribution solution is guaranteed.

Hitherto, CBSM was only applied to a spatially homogeneous setting, in which the General Dynamic Equation (GDE) (Friedlander, 2000) for the size distribution reduces to one dimension, i.e., the size coordinate. This simplifies the presentation significantly, as one is only concerned with the size space, not physical space. Also, we did not consider any coupling of the aerosol processes to the fluid flow. In practice, however, condensation and evaporation will have an effect on pressure, velocity and temperature, indicating that CBSM must be embedded in an algorithm to solve for the dynamics of the flow. In this paper we apply CBSM to a spatially inhomogeneous setting, in which the aerosol mixture is subject to species convection and diffusion. This poses two challenges. First, we would like to retain CBSM’s previously mentioned main strengths in the inhomogeneous setting. Second,

we would like to couple the aerosol dynamics to the dynamics of the flow.

The first challenge is addressed by implementing the fractional step method, allowing to time-integrate the transport equations in multiple steps. This allows to isolate ‘internal’ terms from ‘external’ ones, where ‘internal’ refers to an exclusive dependence on the droplet size. Roughly speaking, we first convect and diffuse, and then nucleate, condense and coagulate. The sum of the internal and external contributions yields, within one time step, an approximate solution at the end of the time step. An additional benefit of this approach is that the time integration of the convective part is not constrained by the explicit integration of the condensational growth as is done in CBSM. In fact, any suitable time integration scheme may be selected to approximate the change of mass concentrations due to convection or diffusion. The second challenge is addressed by a proper integration of CBSM in the compressible PISO algorithm (Frederix, Stanic, Kuczaj, Nordlund, & Geurts, 2015; Issa, 1986; Issa, Ahmadi-Befrui, Beshay, & Gosman, 1991). At both the PISO predictor level and subsequent corrector levels CBSM is taken into consideration, as the condensation and nucleation confront us with transport between different phases, which may lead, on account of the mixture equation of state, to a change in pressure. This possibly drives the flow, and causes a coupling between aerosol processes and fluid transport.

In this paper we apply CBSM to spatially varying flow using the fractional step method. All ‘external’ contributions are time-integrated using the θ -scheme (Morton & Mayers, 2005), formally giving second order accuracy. We apply the method to lid-driven cavity flow. First, the method is validated against incompressible steady state numerical cavity flow solutions of Erturk, Corke, and Gökçöl (2005) and Ghia, Ghia, and Shin (1982). At constant temperature and relatively small Reynolds numbers, we find a very good agreement. Next, we advance to a more specific setting in which an amount of saturated vapor is released in the cavity, while the cavity walls are cooled. This leads to nucleation of droplets near the walls and subsequent condensational growth. We use a logarithmic distribution of sections, such that nucleation may be captured accurately while also the much larger condensational scales are retained accurately. We first study qualitatively the production of aerosol by considering the droplet size distribution along the horizontal and vertical centerlines. We demonstrate that, by using the sectional formulation and the logarithmic distribution of sections, (1) aerosol is captured accurately at small droplet sizes and (2) the droplet size distribution can be completely recovered from the sectional data at any discrete spatial position and in time.

To illustrate the applicability of the method, we also apply the method to aerosol nucleation in a double-mixing tee, in which a hot saturated vapor is diluted by two perpendicular and opposite cold dilution flows. We show that detailed information about the droplet size distribution can be recovered.

The layout of this paper is as follows: in Section 2 a brief introduction of the considered model is presented followed by a detailed description of the numerical method in Section 3. A numerical study of the accuracy and robustness of the method is given in Sections 4 and 5, in which 2D and 3D examples of complex flows with nucleating aerosols are presented. Concluding remarks are collected in Section 6.

2. An Eulerian multi-species sectional aerosol model

In this section we will define the mathematical framework of our model, describing a multi-species aerosol mixture. We follow closely the formulations given in Frederix et al. (2015, 2016), and briefly summarize what is discussed there.

2.1. Equation of state of an aerosol mixture

We consider a mixture consisting of M species. Each species may be present as vapor and liquid droplet. In an arbitrary volume, the mass fraction of the j th species ($1 \leq j \leq M$) in vapor phase is given by Y_j and that in liquid phase by Z_j . By definition,

$$\sum_j (Z_j + Y_j) = 1, \quad (1)$$

where ρY_j and ρZ_j give the mass concentrations of species j in both states present within our arbitrary volume, with ρ being the mean mixture mass density. Following Frederix et al. (2015), it is assumed that liquids are incompressible and that the mass densities of pure constituent, $\rho_j^*(T)$, are known, and depend only on temperature T . For each vapor species, the mass density of pure constituent is given by the product of the compressibility ratio $\psi_j^*(T)$ and pressure, assuming that $\psi_j^*(T)$ is known and only dependent on T . For example, for an ideal gas ψ_j^* is inversely proportional to T .

Assuming that Amagat’s law (Walas, 1985) holds, stating that specific volume is an extensive quantity, we can relate the mixture mass density to pressure as

$$\rho = \psi(p, T)p, \quad (2)$$

with

$$\psi^{-1}(p, T) = \sum_j \frac{Y_j}{\psi_j^*(T)} + p \sum_j \frac{Z_j}{\rho_j^*(T)}. \quad (3)$$

This ‘mean mixture compressibility ratio’ relates pressure to density as a function of p , T and composition. Relation (2) can be considered as the mixture equation of state.

2.2. Mixture mass, momentum and energy transport equations

The dynamics of the vapor–liquid mixture are formulated by incorporating the conservation laws for mass, momentum and energy. Following Frederix et al. (2015) we have:

$$\partial_t \rho + \nabla \cdot (\rho \mathbf{u}) = 0 \quad (4a)$$

$$\partial_t (\rho \mathbf{u}) + \nabla \cdot (\rho \mathbf{u} \mathbf{u}) = -\nabla p + \nabla \cdot (\mu \boldsymbol{\tau}) \quad (4b)$$

$$c_p [\partial_t (\rho T) + \nabla \cdot (\rho T \mathbf{u})] = \nabla \cdot (\kappa \nabla T) + \mu \boldsymbol{\tau} : (\nabla \mathbf{u}) + D_t p, \quad (4c)$$

with ∂_t being the partial derivative to time t , material derivative $D_t := \partial_t + \mathbf{u} \cdot \nabla$, velocity \mathbf{u} , heat capacity at constant pressure c_p , conductivity κ , viscosity μ and rate of strain tensor $\boldsymbol{\tau}$ given by

$$\boldsymbol{\tau} = \nabla \mathbf{u} + (\nabla \mathbf{u})^T - \frac{2}{3} (\nabla \cdot \mathbf{u}) \mathbf{I}, \quad (5)$$

with identity tensor \mathbf{I} . The mixture properties c_p , k and μ are mean properties and assumed to be a mass fraction-weighted sum of all corresponding species-specific properties, e.g., $\kappa = \sum_j (\kappa_{v,j}^* Y_j + \kappa_{l,j}^* Z_j)$ with $\kappa_{v,j}^*$ and $\kappa_{l,j}^*$ being the conductivity of pure constituent j in vapor and liquid state, respectively. The validity of this choice is debatable, however, due to the low mass and volume fractions of our phase-changing species in the remainder of this paper, this assumption is reasonable.

Eq. (4c) assumes that a unique temperature T exists describing the local temperature of the mixture entirely. This makes the description of the mixture isothermal; both vapor and droplet phase have locally the same temperature and heat transfer is assumed to take place sufficiently rapidly. This is a reasonable assumption if temperature differences are kept moderate and if the aerosol mixture is dilute, which will be the case in the remainder of this paper. However, in some cases a non-isothermal description may be required. The properties of the droplet phase should be determined using a slightly different temperature than that of the vapor phase, due to energy transfer taking place insufficiently rapidly, with vapor and liquid not in mutual equilibrium. Such an approach could be implemented in our framework, by separating the vapor temperature from the droplet temperature. In fact, the droplet temperature could become size-dependent. For both temperatures, then, transport equations may be formulated taking into account the non-isothermal heat transfer in between both phases. However, we consider a proper discussion of this to lay beyond the scope of this work.

We can expand (4a) for each species, giving

$$\partial_t (\rho Y_j) = -\nabla \cdot (\rho Y_j \mathbf{u}) - \nabla \cdot (\rho Y_j \mathbf{v}_j) - S_j \quad (6a)$$

$$\partial_t (\rho Z_j) = -\nabla \cdot (\rho Z_j \mathbf{u}) + S_j, \quad (6b)$$

with the j th species ‘diffusive velocity’ \mathbf{v}_j and vapor-to-liquid mass transfer rate S_j . It is assumed that the liquid droplets, given their relatively large mean size with respect to the size of molecules, do not diffuse. If we sum (6a) and (6b) for each species, and using (1), we find (4a) provided

$$\rho \sum_j Y_j \mathbf{v}_j = 0, \quad (7)$$

i.e., the net diffusive flux is zero. Following Giovangigli (1991), we adopt ‘Hirschfelder–Curtiss approximated diffusion’, in which the species-specific diffusive velocity takes the shape

$$\mathbf{v}_j = -\frac{D_j^*}{X_j} \nabla X_j + \mathbf{u}_c, \quad (8)$$

with D_j^* being the j th species diffusion coefficient (see Giovangigli, 1991), vapor mole fraction X_j and \mathbf{u}_c the species-independent correction velocity. This correction velocity gives an artificial degree of freedom to later impose (7). Since the j th species mole fraction relates to the mass fraction as $X_j = Y_j Q / Q_j$ with Q being the ‘molar mean molecular weight’ of the mixture (in units of kg/mole) and Q_j its constant species-specific counterpart, (8) may be written as

$$\mathbf{v}_j = -\frac{D_j^*}{Y_j} \nabla Y_j - \frac{D_j^*}{Q} \nabla Q + \mathbf{u}_c \approx -\frac{D_j^*}{Y_j} \nabla Y_j + \mathbf{u}_c. \quad (9)$$

Since we only consider mixtures with an abundant carrier gas and small concentrations of vapor or liquid, Q will only vary weakly in space which allows for the approximation in (9) of neglecting the ∇Q term. The correction velocity \mathbf{u}_c follows directly from requirement (7), by plugging in (9).

2.3. The droplet size distribution and its sectional representation

We assume an ‘internally mixed’ (Friedlander, 2000) aerosol, i.e., composition is locally independent of the droplet size. Using a new independent variable z giving the mass of a droplet, the droplet size distribution $n(\mathbf{x}, z, t)$ is introduced, defined such that $n(\mathbf{x}, z, t) dz$ is the total number of droplets per unit of volume having size $[z, z + dz]$, at position $\mathbf{x} = (x_1, x_2, x_3)$ and time t , see Ramkrishna (2000). The droplet size distribution adheres to the well-known General Dynamic Equation (GDE) (Friedlander, 2000)

for particle transport, condensation and nucleation:

$$\partial_t n(\mathbf{x}, z, t) = -\nabla \cdot (n(\mathbf{x}, z, t) \mathbf{u}) - \partial_z (I(z, t) n(\mathbf{x}, z, t)) + J_{\text{nuc}}(\mathbf{x}, t) \delta(z - z_{\text{nuc}}(t)) + J_{\text{coa}}(\mathbf{x}, z, t), \quad (10)$$

with $I(z, t) = \sum_j I_j(z, t)$ being the rate of change of a z -sized droplet through condensation, $J_{\text{nuc}}(\mathbf{x}, t)$ the nucleation rate, $z_{\text{nuc}}(t)$ the mass of nucleating droplets and $J_{\text{coa}}(\mathbf{x}, z, t)$ the coagulation term.

The droplet size distribution may also be formulated in a sectional context. This means that a finite sized domain is divided into P arbitrarily sized adjoining intervals. The i th section (with $0 \leq i \leq P - 1$) is representative for droplets of size $y_i < z < y_{i+1}$, with y_i being the position of the sectional interface between the $(i - 1)$ th and the i th section. Each section contains a representative size z_i , $y_i < z_i < y_{i+1}$, to which all droplets are assigned. This allows to write the size distribution as a finite sum of Dirac delta functions, each centered around a unique representative size z_i :

$$n(\mathbf{x}, z, t) = \sum_i N_i \delta(z - z_i) dz, \quad (11)$$

where N_i is the total number of droplets per unit of volume in section i , i.e.,

$$N_i = \int_{y_i}^{y_{i+1}} n(\mathbf{x}, z, t). \quad (12)$$

We now have two quantities describing the liquid phase: the j th species liquid concentration ρZ_j and the concentration $n(\mathbf{x}, z, t) dz$ of droplets having mass $[z, z + dz]$. Inevitably, both descriptions of the droplets contain information about the total amount of liquid in the system. This leads to a redundancy; the droplet size distribution is subject to the following constraint:

$$\rho \sum_j Z_j = \int_0^\infty zn(\mathbf{x}, z, t) dz, \quad (13)$$

i.e., the first moment of the droplet size distribution (with z being the droplet mass) must reflect the total liquid mass in the system. We will verify this constraint in the simulations run in [Sections 4 and 5](#).

2.4. Nucleation, condensation and coagulation source terms

In the previous two sections we have introduced several source terms which are yet to be specified. The j th species vapor-to-liquid mass transfer rate S_j contains the contributions of condensation and nucleation, i.e., $S_j = S_{\text{cond},j} + S_{\text{nuc},j}$. As shown in [Frederix et al. \(2016\)](#), these are related to the j th species z -sized droplet condensation rate $I_j(z, t)$ and nucleation rate $J_{\text{nuc}}(\mathbf{x}, t)$ as

$$S_{\text{cond},j} = \int_0^\infty I_j(z, t) n(\mathbf{x}, z, t) dz \quad (14a)$$

$$S_{\text{nuc},j} = z_{\text{nuc},j}(t) J_{\text{nuc}}(\mathbf{x}, t), \quad (14b)$$

with $z_{\text{nuc},j}$ being the mass of species j in a so-called critical cluster of nucleation.

The coagulation source term in (10) is, in the limit of a continuous distribution, given by ([Friedlander, 2000](#)):

$$J_{\text{coa}}(\mathbf{x}, z, t) = \frac{1}{2} \int_0^z \beta(\tilde{z}, z - \tilde{z}) n(\tilde{z}, t) n(\mathbf{x}, z - \tilde{z}, t) d\tilde{z} - \int_0^\infty \beta(z, \tilde{z}) n(\mathbf{x}, z, t) n(\tilde{z}, t) d\tilde{z}, \quad (15)$$

in which the first integral accounts for freshly created z -sized droplets by coagulation of two smaller droplets, the second integral for the removal of z -sized droplets by coagulation with any other droplet and $\beta(z_1, z_2)$ the coagulation kernel for the coagulation of a z_1 -sized and z_2 -sized droplet. For the coagulation kernel we adopt the description given by [Lee and Chen \(1984\)](#). What remains is the specification of $I_j(z, t)$, $J_{\text{nuc}}(\mathbf{x}, t)$ and $z_{\text{nuc},j}$. Following [Wilck and Stratmann \(1997\)](#), the condensation rate is given by

$$I_j(z, t) = 2\pi D_j^* d(z) \rho f(Kn) Y_j^s (S_j^s - E_j), \quad (16)$$

with $d(z)$ being the droplet diameter of a z -sized droplet, Y_j^s the equilibrium vapor mass fraction over a flat surface and S_j^s the saturation ratio. Both the ‘transition function’ $f(Kn)$ and the Kelvin effect factor E_j are here, for mathematical convenience, set to unity. The multi-species nucleation rate is given in [Winkelmann, Kuczaj, Nordlund, and Geurts \(2016\)](#).

3. Extension of the characteristics-based sectional method to a spatially varying setting

In this section the well-known compressible PISO method is extended to incorporate CBSM, originally presented in [Frederix et al. \(2016\)](#). There the GDE was reduced to a spatially homogeneous setting, which allows to incorporate the analytic solution of the hyperbolic condensation equation in the z -space. To use the techniques presented in [Frederix et al. \(2016\)](#) without further modification, we must isolate the spatially independent (i.e., independent with respect to physical space) contributions in (6a), (6b) and (10) from the spatial ones. We use the fractional step method for this, incrementally ‘adding’ each right-hand side contribution to the solution.

3.1. Fractional steps in the θ -method

Let us consider the following abstract PDE:

$$\partial_t u(\mathbf{x}, t) = f_1(u(\mathbf{x}, t)) + f_2(u(\mathbf{x}, t)), \quad (17)$$

in which the rate of change of an unknown $u(\mathbf{x}, t)$ depends on two source terms f_1 and f_2 , representing spatially dependent (e.g., convection and diffusion) and spatially independent (e.g., condensation, nucleation and coagulation) sources, respectively. We would like to time-integrate the contribution of f_1 with the θ -scheme (Morton & Mayers, 2005), in which the contribution of f_1 is evaluated by a fraction of θ at the new time level and a fraction of $(1 - \theta)$ at the old time level. This allows for second order convergence if $\theta = \frac{1}{2}$ (Morton & Mayers, 2005). The contribution of f_2 is taken explicitly. This choice is motivated by the fact that CBSM treats condensational growth and nucleation explicitly. We find

$$\frac{u^{m+1} - u^m}{\Delta t} = \theta f_1(u^{m+1}) + (1 - \theta)f_1(u^m) + f_2(u^m), \quad (18)$$

where u is discretized in time on t^m and $t^{m+1} = t^m + \Delta t$. Equivalent to (18) we can find u^{m+1} in two fractional steps:

$$\frac{\tilde{u}^{m+1} - u^m}{\Delta t} = \theta f_1(u^{m+1}) + (1 - \theta)f_1(u^m) \quad (19a)$$

$$\frac{u^{m+1} - \tilde{u}^{m+1}}{\Delta t} = f_2(u^m), \quad (19b)$$

where \tilde{u}^{m+1} is an intermediate solution. It is easy to verify that when \tilde{u}^{m+1} is eliminated from (19), Eq. (18) is obtained. The fractional step-form allows for the implementation of two separate solution algorithms, e.g., CBSM can be used to solve (19b). Note, however, that (19a) represents a three-point scheme in time if $\theta > 0$ yielding unknowns at time level t^{m+1} and intermediate time \tilde{t}^{m+1} . If one wants to successively solve (19a) and (19b)—which is desirable here, to implement CBSM—the $f_1(u^{m+1})$ contribution must be iteratively updated by a previous iterative solution of (19b) for u^{m+1} . Let the superscript k denote the iteration level, with $1 \leq k \leq N_p$. We then propose the following iterative scheme:

$$\frac{\tilde{u}^{m+1,k} - u^m}{\Delta t} = \theta f_1(u^{m+1,k-1}) + (1 - \theta)f_1(u^m) \quad (20a)$$

$$\frac{u^{m+1,k} - \tilde{u}^{m+1,k}}{\Delta t} = f_2(u^m). \quad (20b)$$

For $k=1$ (the first iteration) $u^{m+1,k-1}$ in (20a) is unavailable and we set this term to $\tilde{u}^{m+1,k}$, meaning that for the first iteration (20a) becomes implicit with respect to $\tilde{u}^{m+1,k}$. This choice will be motivated later. For $k > 1$ the first term in the right-hand side of (20a) is explicitly computed using the solution for u at the previous iteration. At the final iteration the solution is accepted as the ‘final answer’, i.e., $u^{m+1} = u^{m+1,N_p}$. If the scheme converges (which was the case in all studied settings in this paper), then for $k \rightarrow \infty$ we have $u^{m+1,k} = u^{m+1,k-1}$, i.e., the solution at two consecutive iteration levels are equal and converged. In that case the form (20) becomes equal to the ‘exact’ form (19).

3.2. Implementation of the fractional step method in PISO

In the compressible PISO algorithm for reacting flows a solution is found to the set of equations (4) in a segregated way, by means of an implicit predictor step and a number of corrector steps, see Issa et al. (1991) and Frederix et al. (2016). The fact that iterations are required to find an acceptable solution allows to integrate the θ -method-based fractional step scheme in a straightforward way. Let us consider (1) the j th species mass fraction transport equations, written in short-hand notation as:

$$\partial_t(\rho Y_j) = f_1(Y_j) + f_2(Y_j) \quad (21a)$$

$$\partial_t(\rho Z_j) = g_1(Z_j) + g_2(Z_j), \quad (21b)$$

where $f_1(Y_j)$ and $g_1(Z_j)$ contain the effects of spatial convection–diffusion and $f_2(Y_j)$ and $g_2(Z_j)$ the effects of condensation–nucleation, and (2) the GDE written as

$$\partial_t n = h_1(n) + h_2(n) + h_3(n), \quad (22)$$

with $h_1(n)$, $h_2(n)$ and $h_3(n)$ being the effects of spatial convection, condensation–nucleation and coagulation, respectively. The solution of the mass fractions is strongly coupled to pressure through, for example, the mixture compressibility ratio (3). This means that (21) must be incorporated into PISO. Following closely the scheme proposed in the previous section, we again use iterative level superscript k where $k=1$ now is the so-called implicit predictor step and $k > 1$ are the *explicit corrector steps*. Using

$$\frac{\rho^{m+1,k-1} \tilde{Y}_j^{m+1,k} - \rho^m Y_j^m}{\Delta t} = \theta f_1(Y_j^{m+1,k-1}) + (1 - \theta)f_1(Y_j^m) \quad (23a)$$

$$\rho^{m+1,k-1} \frac{Y_j^{m+1,k} - \tilde{Y}_j^{m+1,k}}{\Delta t} = f_2(Y_j^m). \tag{23b}$$

we propose the following algorithm:

- *Implicit predictor step, $k=1$.* In (23a) we set $Y_j^{m+1,k-1} = \tilde{Y}_j^{m+1,k}$, making (23a) implicit with respect to $\tilde{Y}_j^{m+1,k}$. This choice extends from the idea that in PISO first an implicit predictor is performed. Also, due to this choice (23) reduces to the exact PISO form when $f_2 = 0$. Density $\rho^{m+1,k-1}$ is set to ρ^m in agreement with PISO.
- *Explicit corrector steps, $k > 1$.* Before solving Eq. (23) the mixture compressibility is updated and the pressure equation is solved to find a corrected pressure $\rho^{m+1,k-1}$ and density $\rho^{m+1,k-1}$, see Issa et al. (1991). This density is used to find $Y_j^{m+1,k}$ solving (23a) and (23b) successively, while applying CBSM to (23b). The corrector step is repeated multiple times until one or more convergence criteria of choice are satisfied. The latest iteration $Y_j^{m+1,k}$ is accepted as the final solution Y_j^{m+1} . As the number of iterations k increases, the convection–diffusion source term f_1 at the new time level, although explicitly evaluated with $Y_j^{m+1,k-1}$, approaches time level $m + 1$. It is easy to verify then that eliminating $\tilde{Y}_j^{m+1,k}$ from (23) gives a close approximation to the desired form.

In an obvious and similar way this approach is applied to integrate Eqs. (21b) and (22) into PISO, with the only difference that the coagulation source term h_3 in Eq. (22) is incorporated in a third fractional step which is performed only once after the PISO correctors. As coagulation has no effect on the mixture properties (mass fractions remain the same), coagulation creates no coupling with other equations, and can therefore be solved separately. For this, we use the method as proposed by Kumar and Ramkrishna (1996), which integrates seamlessly with the proposed sectional formulation.

Rather than solving the GDE in terms of $n(\mathbf{x}, z, t)$, we solve it for N_i , by taking the integral of the GDE with respect to z over each section. The GDE, without the effects of nucleation, condensation and coagulation, then takes the form

$$\partial_t N_i + \nabla \cdot (N_i \mathbf{u}) = 0 \tag{24}$$

For the discretization of all transport equations we embrace the finite volume framework as implemented in OpenFOAM®. Using Gauss's theorem, the divergence terms and Laplacians are rewritten to cell-surface integrals. As OpenFOAM offers a collocated cell-centered framework, we must interpolate to the cell faces. For the Laplacian terms, as well as the divergence terms for velocity and temperature and the gradient of pressure, we use the linear interpolation scheme.

The diffusion term in (6a) can, using (9), be written as

$$\nabla \cdot (\rho Y_j \mathbf{v}_j) = \nabla \cdot (\rho D_j^* \nabla Y_j) + \nabla \cdot (\rho Y_j \mathbf{u}_c). \tag{25}$$

For consistency with the treatment of the Laplacian in the right-hand side, the second term in the right-hand side is also discretized using linear interpolation to the face.

For the treatment of the divergence terms for the Y_j , Z_j and N_i transport equations, we prefer, out of physical considerations, a positivity-preserving scheme. The central scheme is known to allow negativity. Apart from the upwind scheme, there are numerous limiter schemes available in OpenFOAM which preserve positivity. These schemes locally reduce to an upwind interpolation, depending on the local ratio of successive gradients of the solution such that the solution remains total variation diminishing. However, the limiter function may yield a different value for each Y_j , Z_j and N_i , adding different amounts of diffusion per solution field. This means that different interpolations are used, breaking consistency in terms of (1) and (13). A ‘global’ limiter should be designed, yielding the same limiter value for each field. However, this is beyond the scope of this paper. Therefore, we adopt the upwind scheme for the interpolation in the divergence terms for Y_j , Z_j and N_i , giving a diffusive but consistent and non-negative

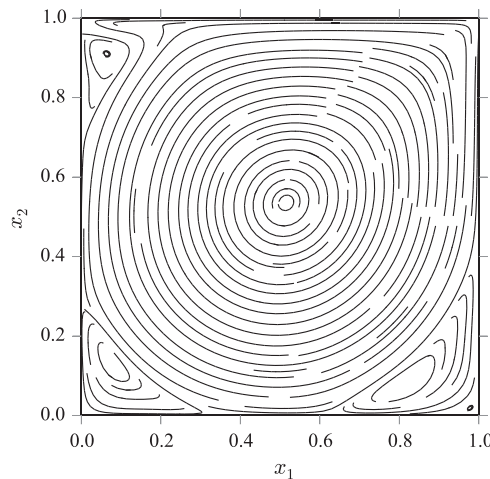


Fig. 1. Streamlines of the steady state solution for $Re=5000$. The simulation was run using a uniform 256^2 grid, and $\max(CFL) = 0.5$.

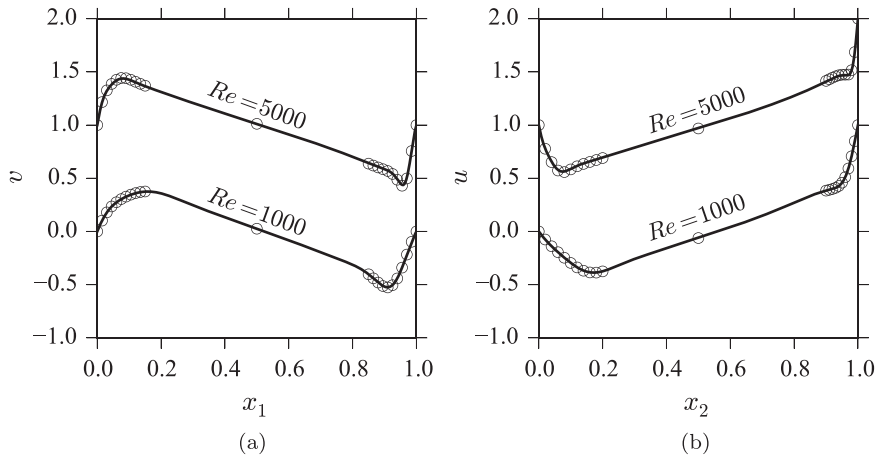


Fig. 2. (a) The y -component of the velocity along the horizontal centerline and (b) the x -component of the velocity along the vertical centerline, for two Reynolds numbers. The data points (circles) are taken from [Erturk et al. \(2005\)](#). The simulations were run using a 256^2 grid, and $\max(\text{CFL}) = 0.5$. The curves for $Re=5000$ are elevated by 1 for visual clarity.

solution.

The PISO convergence criterion is based on the pressure equation residual as defined in [Frederix et al. \(2015\)](#), which is

$$r_p = \frac{1}{N_c} \left\| \frac{\mathbf{b} - \mathbf{A}\mathbf{p}^{k-1}}{\text{diag}(\mathbf{A})} \right\|, \quad (26)$$

with N_c being the number of cells, coefficient matrix \mathbf{A} and source \mathbf{b} of the fully discretized pressure equation, \mathbf{p}^{k-1} the latest iteration of the pressure solution and $\|\cdot\|$ the L_1 -norm. The residual r_p tells us how well the pressure equation is satisfied. In the remainder of this text we set the PISO convergence criterion to 10^{-7} Pa, which was shown to be sufficient in [Frederix et al. \(2015\)](#). Since the total pressure is in the order of 10^5 Pa, this convergence criterion gives, roughly speaking, a precision of approximately 12 decimals in p . For practical purposes this is an unnecessarily large reduction of the splitting error. However, for the resolution studies presented later on, this high accuracy avoids that the splitting error ‘overshadows’ the temporal and spatial discretization errors.

For the time discretization we set $\theta = \frac{1}{2}$, effectively yielding the Crank–Nicolson scheme ([Morton & Mayers, 2005](#)).

4. Aerosol formation and transport in two-dimensional lid-driven cavity flow

In this section the aerosol model and the PISO-integrated CBSM are applied to the canonical problem of two-dimensional lid-driven cavity flow. This problem is well known, and extensively studied in the literature concerning steady flow in an incompressible context. Although we assume a compressible description of the flow, in the limit of isothermal low Mach flow our steady state solutions are expected to be close to the incompressible ones. [Ghia et al. \(1982\)](#) provide accurate steady state numerical solutions for incompressible cavity flow at various Reynolds numbers. Many other authors have done similar studies, see for example [Erturk et al. \(2005\)](#) for an overview. These benchmark data allow for a validation of our numerical solution of the lid-driven cavity flow.

Having established a foundation for the steady-state solution, we study the transient flow, starting from a quiescent state, and include the formation, evolution and transport of aerosol. Using a typical case, the aerosol processes are illustrated and the resulting droplet size distributions are studied. We investigate dependence of the solution, in terms of the formed aerosol, on the CBSM scheme, number of sections P , time step size Δt and grid cell size Δx . The study of this problem assists in (1) establishing confidence in the method and (2) to show control of the numerical error.

4.1. Validation of two-dimensional cavity flow against benchmark data

In the remainder of this section we consider the benchmark data as presented by [Erturk et al. \(2005\)](#). Their data was, in turn, validated against those of [Ghia et al. \(1982\)](#). We consider $Re=1000$ and $Re=5000$.

Table 1

Convergence of e_{hor} and e_{ver} for a grid cell size sequence, using a 512^2 mesh as reference solution at $Re=1000$.

Grid	e_{hor}	Order	e_{ver}	Order
32^2	0.1665		0.1448	
64^2	0.0496	1.832	0.0440	1.814
128^2	0.0133	1.931	0.0119	1.926
256^2	0.0027	2.213	0.0024	2.213

Table 2List of initial conditions (IC) and boundary conditions (BC) for the cavity. The BCs apply for $\mathbf{x} = (x_1, 0)$, (x_1, L) , $(0, x_2)$, (L, x_2) .

Variable	IC	BC
T (K)	T_0	T_∞
\mathbf{u} (m/s)	$(0, 0)$	$(1, 0)$ for $x_2 = L$, $(0, 0)$ for $x_2 \neq L$
p (Pa)	10^5	Zero gradient
Z_{DBP}	0	Zero gradient
N_i (m^{-3})	0	Zero gradient
Y_{DBP}	$Y_{\text{DBP}}^s(T_0)f(\mathbf{x})$	Zero gradient
Y_{air}	$1 - Y_{\text{DBP}}$	Zero gradient

Fig. 1 shows the typical geometry of the lid-driven cavity. The size of the cavity is here set to $L=1$ m. Moreover, the velocity of the lid is set to $\mathbf{u} = (1, 0)$ m/s. If we set the density of the fluid inside the cavity to unity too, the definition of the Reynolds number reduces to $Re=1/\mu$. By setting the viscosity of the fluid we have control over the flow Reynolds number.

We specify no-slip boundary conditions for velocity and zero-gradient boundary conditions for pressure. At $t=0$ s we have $\mathbf{u} = 0$ m/s and set the lid in motion instantly. Temperature is kept uniform at the walls.

Fig. 1 shows the steady state streamlines of the flow for $Re=5000$, at constant temperature, computed using a uniform 256^2 grid and a variable time step size Δt restricted by $\max(\text{CFL}) = 0.5$. Qualitatively, the three corner vortices resemble those shown in Erturk et al. (2005) well. Fig. 2 shows the perpendicular velocity at the horizontal and vertical centerlines of the cavity flow, at steady state for $Re=1000$ and $Re=5000$, along with data points from Erturk et al. (2005). Even though we adopt a compressible formulation, a good visual agreement is found between our simulated flow and the incompressible steady state solutions of Erturk et al. (2005).

The previous results were obtained using a uniform 256^2 grid. To assess the quality of the grid, we introduce convergence measures e_{hor} and e_{ver} , defined as

$$e_{\text{hor}}^2 = \frac{\int_0^L (v - v_{\text{ref}})^2 dx}{\int_0^L v_{\text{ref}}^2 dx} \quad (27a)$$

$$e_{\text{ver}}^2 = \frac{\int_0^L (u - u_{\text{ref}})^2 dy}{\int_0^L u_{\text{ref}}^2 dy}, \quad (27b)$$

where $\mathbf{u} = (u, v)$ and \mathbf{u}_{ref} a reference solution. Eq. (27a) is evaluated at $y = L/2$ and Eq. (27b) at $x = L/2$. Table 1 shows e_{hor} and e_{ver} for four different grids, with respect to a reference solution taken at a fine uniform 512^2 grid. Both measures decrease approximately at second order with an increase in the number of grid points. For the 128^2 grid both convergence measures are approximately 1%, indicating that the solution for velocity is, with respect to the chosen grid, represented quite accurately.

4.2. Aerosol production, evolution and transport in lid-driven cavity flow

Having studied and validated the solution of our method for the isothermal flow problem, we now introduce aerosol formation through nucleation, aerosol evolution through condensation and aerosol transport. We do this by starting with a quiescent state in which a certain amount of vapor is present. As the lid of the cavity sets the mixture in motion, it is also cooled by an imposed lower boundary temperature. Conditions are such that the vapor becomes supersaturated, allowing for nucleation and subsequent condensational droplet growth. We consider, for convenience, a single-species mixture of DBP (Dibutyl Phthalate) vapor with air. Rather than subscript j , we use $_{\text{air}}$ and $_{\text{DBP}}$ to denote species-specific variables. We use the physicochemical properties as specified in Frederix et al. (2015).

Table 2 shows a list of initial and boundary conditions. The mixture, initially at $T_0 = 373.15$ K, is cooled by setting the temperature of the walls to $T_\infty = 273.15$ K at $t=0$. At $T = T_0$ the saturation mass fraction of DBP in air is given by $Y_{\text{DBP}}^s(T_0)$. To avoid heavy aerosol formation at the wall, Y_{DBP} is initially set to $Y_{\text{DBP}}^s(T_0)$ weighted by a scaling field $f(\mathbf{x})$, adhering to

$$f(\mathbf{x}) = \max\left(1 - \frac{2|\mathbf{x} - \mathbf{x}_c|}{L}, 0\right), \quad (28)$$

with $\mathbf{x}_c = \frac{1}{2}(L, L)$. This creates a ‘cone’ of vapor concentration with zero vapor concentration at the walls. Through vapor diffusion, however, nucleation is still expected to occur at the wall.

The mass of DBP is small for the given initial conditions ($\max(Y_{\text{DBP}}) \approx 8.65 \cdot 10^{-4}$). If we approximate the mixture as pure air, then using the physicochemical properties given in Frederix et al. (2015) the Reynolds number of the flow becomes $Re=1.927 \cdot 10^7 L/T$. We set $L=0.075$ m to achieve a Reynolds number of approximately 5000 at lower temperatures.

In classical nucleation theory the mass of nucleation z_{nuc} , also referred to as the critical cluster or nucleus size, is given by (Friedlander, 2000):

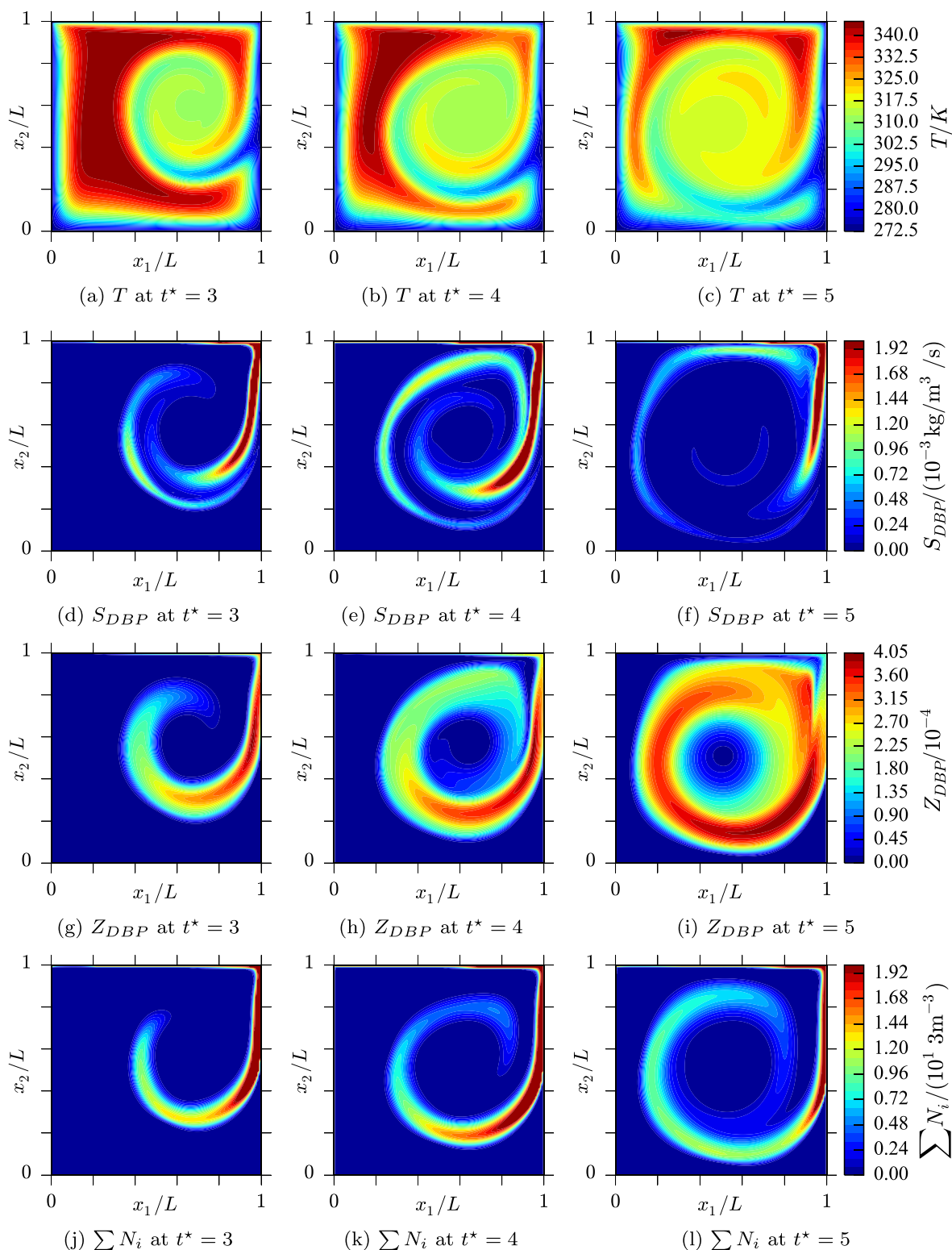


Fig. 3. At $t^* = 3, t^* = 4$ and $t^* = 5$ (from left to right) the contour maps of the two-dimensional cavity for temperature, condensation rate, liquid mass fraction and total droplet number concentration (from top to bottom) are shown. The simulations were performed on a 128^2 grid using $\Delta t = 16 \cdot 10^{-5} \text{ s}$, $P=8$ sections/decade and the hybrid CBSM scheme. Only one colorbar is shown for each quantity.

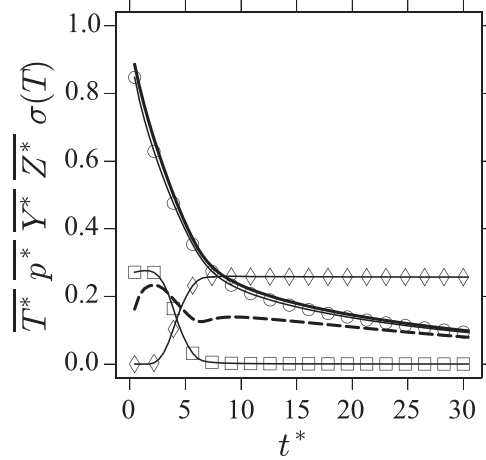


Fig. 4. Spatial averages of T^* (solid black), p^* (circles), Z^* (diamonds) and Y^* (squares), and spatial standard deviation of T^* (dashed), as a function of dimensioned time.

$$z_{\text{nuc}} = \frac{\pi}{6} \left(\frac{4\sigma V_m}{\ln(S^s) k_B T} \right)^3 \rho_{\text{DBP}}^* \tag{29}$$

where σ is the surface tension, V_m the molecular volume, S^s the saturation ratio and k_B the Boltzmann constant. When saturation is large the critical cluster size decreases. Theoretically, the max saturation which may be achieved is $\max S^s = Y_{\text{DBP}}^s(T_0)/Y_{\text{DBP}}^s(T_\infty)$, i.e., in the case of an instant cooling from T_0 to T_∞ at \mathbf{x}_c . Using this together with Eq. (29) gives an estimate for the smallest droplet sizes which we must resolve in order to capture nucleation. In our setting, $\min(z_{\text{nuc}})$ is approximately 10^{-24} kg. In practice it suffices to set

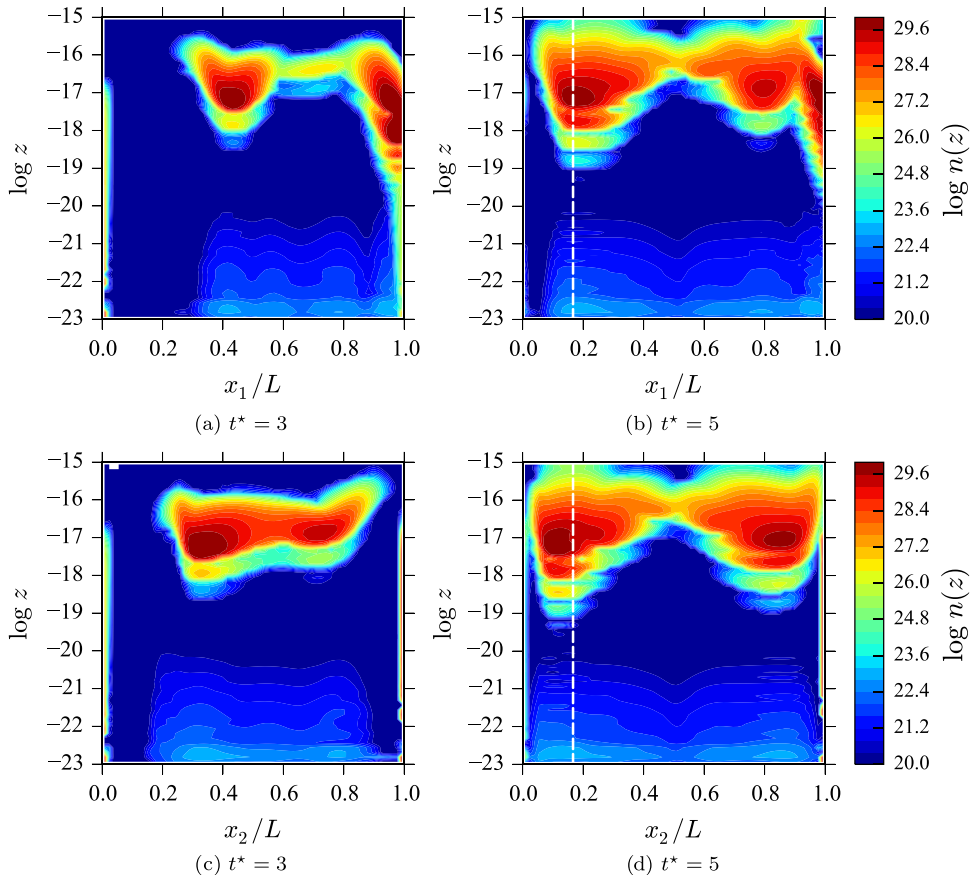


Fig. 5. The logarithm of the droplet size distribution on the horizontal centerline (top row) and vertical centerline (bottom row) at two times. The dashed lines in (b) and (d) correspond to $x = (L/6, L/2)$ and $x = (L/2, L/6)$, the two positions used in Figs. 7 and 8.

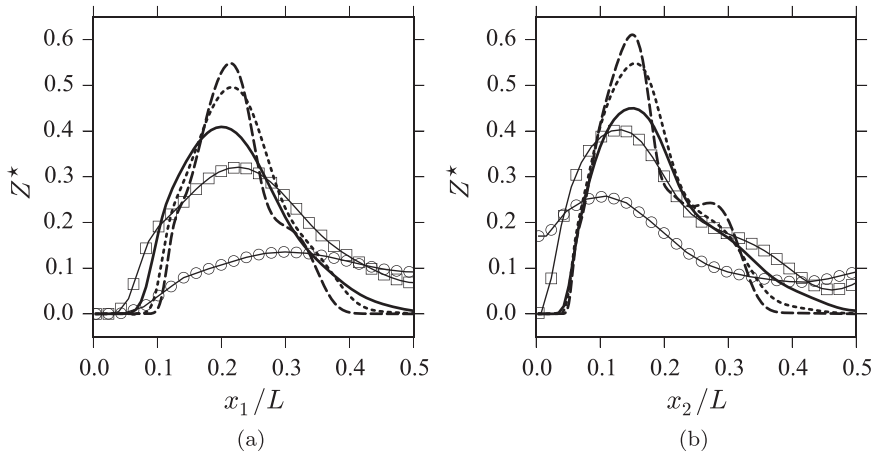


Fig. 6. DBP mass fraction Z_{DBP} of the (a) horizontal and (b) vertical centerline at $t^* = 5$ for a 32^2 (circles), 64^2 (squares), 128^2 (solid), 256^2 (dotted) and 512^2 (dashed) grid. The simulation was run with $P=8$ sections/decade and $\Delta t = 16 \cdot 10^{-5}$ s. Only the first half of the centerlines are shown, for visual clarity.

the lower boundary of the first section, i.e., y_0 , to 10^{-23} kg. An estimate for the upper boundary of the last section is more difficult to make, since the maximum droplet size depends on a complex interaction of nucleation, condensation and coagulation, which, in turn, depend on a non-trivial development of the temperature and flow in the cavity. In the remainder of this section we set the upper boundary of the last section to $y_p = 10^{-15}$ kg. We verified that for this setting less than 1% of the droplet mass grows beyond this size. Given the large range in possible droplet scales, i.e., $10^{-23} \leq z \leq 10^{-15}$, we use a logarithmic distribution of section sizes and

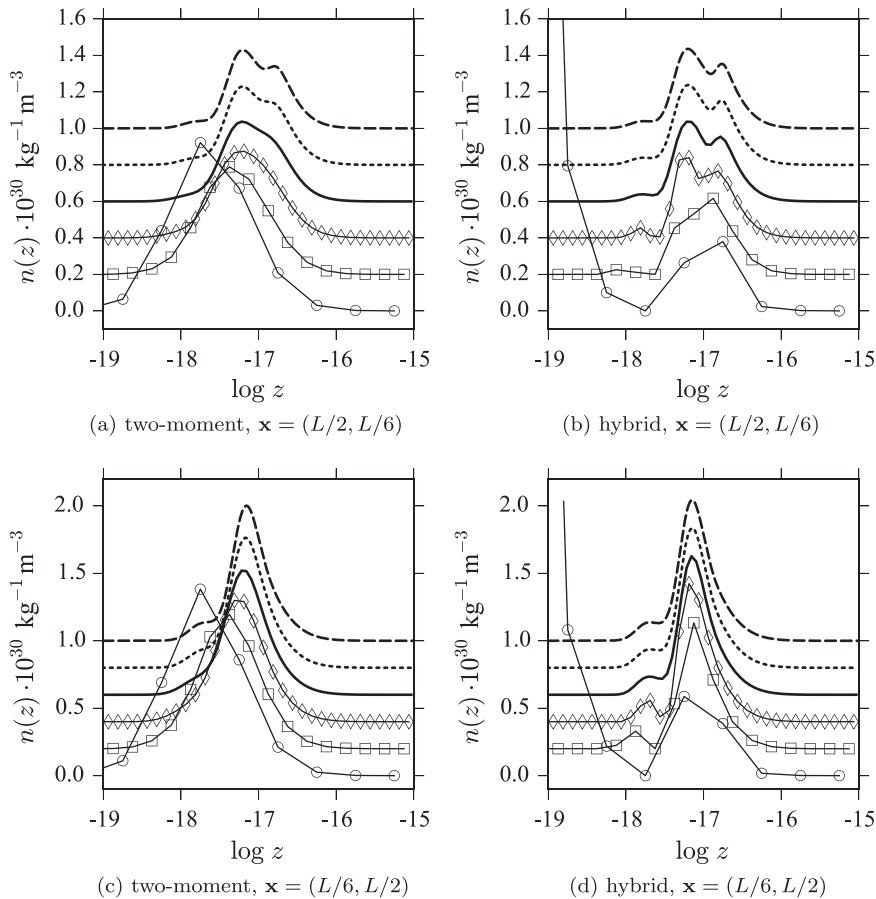


Fig. 7. Droplet size distribution at $t^* = 5$ for 2 (circles), 4 (squares), 8 (diamonds), 16 (solid), 32 (dotted) and 64 (dashed) sections/decade. Each line in this sequence has a vertical offset of $2 \cdot 10^{29}$ with respect to the previous ones, for visual clarity. The left column shows results for the two-moment CBSM scheme, the right column for the hybrid CBSM scheme, the top row at $\mathbf{x} = (L/2, L/6)$, the bottom row at $\mathbf{x} = (L/6, L/2)$. In all figures the grid was 128^2 and $\Delta t = 16 \cdot 10^{-5}$ s.

assign a fixed number of sections per decade. This was shown to give good results for capturing spatially homogeneous nucleation and condensation in Frederix et al. (2016).

Fig. 3 shows development of the temperature and aerosol mixture at three instants $t^* = 3, 4, 5$, where t^* is the non-dimensional time, defined as

$$t^* = \frac{tU}{\pi L}, \tag{30}$$

i.e., the time t scaled by the approximate time of one revolution in the steady state. In this equation U is the magnitude of the velocity of the cavity lid. The flow transports the vapor to the right wall, at which nucleation and subsequent condensation starts, enabled by the lower temperature near the wall. At $t^* \approx 3$, the initially generated aerosol droplets complete a rotation through the cavity. We verified that for $t \rightarrow \infty$, the mean temperature reduces to T_∞ . Moreover, because of the dependence of density on temperature, the pressure drops too.

Fig. 4 shows the spatial average of the scaled temperature $\overline{T^*}$, scaled pressure $\overline{p^*}$, scaled DBP vapor and liquid mass fractions $\overline{Y^*}$ and $\overline{Z^*}$, respectively, and the standard deviation of the scaled temperature, $\sigma(T^*)$, all as a function of scaled time t^* . These scaled quantities are defined as follows:

$$T^* = \frac{T - T_\infty}{T_0 - T_\infty}, \quad p^* = \frac{p - p_\infty}{p_0 - p_\infty}, \quad Y^* = \frac{Y_{\text{DBP}}}{Y_0}, \quad Z^* = \frac{Z_{\text{DBP}}}{Y_0}, \tag{31}$$

with p_0 being the initial pressure, p_∞ the static pressure of the mixture at T_∞ and Y_0 the saturation mass fraction of DBP at T_0 . Both the spatially averaged pressure and temperature are shown to decrease towards their theoretical steady state solutions T_∞ and p_∞ , or, $T^* = 0$ and $p^* = 0$. The standard deviation of temperature also decreases, albeit slowly. The majority of the exchange of DBP vapor to liquid droplets occurs within the first two time units, as is shown by the spatial averages of Y^* and Z^* .

In each computational cell and at any discrete time the droplet size distribution, expressed in sections, is known. From the sectional data the four-dimensional droplet size distribution $n(\mathbf{x}, z, t)$ may be reconstructed using Eq. (12), representing n as piecewise constant in each section. Fig. 5 shows n in the $(x_1, \log z)$ -plane across the horizontal centerline, and $n(x, z, t)$ in the $(x_2, \log z)$ -plane across the vertical centerline, for $t^* = 3.5$. A clear development of the distributions along the two centerlines is apparent. At the right wall the majority of the droplets reside in smaller size classes, and they appear to grow to larger ones while moving into the domain and passing the vertical centerline. Moreover, the matured droplet size distributions at later times show multiple ‘layers’, see the dashed lines in Fig. 5b and d. These layers are the result of the time-dependent behavior of the solution: they can be viewed as an aggregate of droplet nucleation and condensation over time. Due to the interaction of both flow and nucleation with subsequent condensation, the droplet size distribution at a point in time and space becomes non-trivial and may accumulate contributions from different past times of cyclic motion in the cavity. At the walls, in particular at $t^* = 3$ in Fig. 5, diffusion-driven droplet nucleation is shown.

4.3. Sensitivity of the solution to Δt , Δx and the number of sections

In the previous section we have shown a number of results for a typical lid-driven cavity simulation on a 128^2 grid, a time step size of $\Delta t = 16 \cdot 10^{-5}$ s and an 8 sections/decade sectional distribution. The question remains: how accurate are these results and do we have control over the numerical error? This will be addressed in this section.

First, we investigate the grid dependence of the solution. Fig. 6 shows, for a sequence of 5 grids, the horizontal and vertical centerline solutions for the mass fraction of DBP, Z_{DBP} , for fixed P and Δt . The solution changes considerably as the grid is refined,

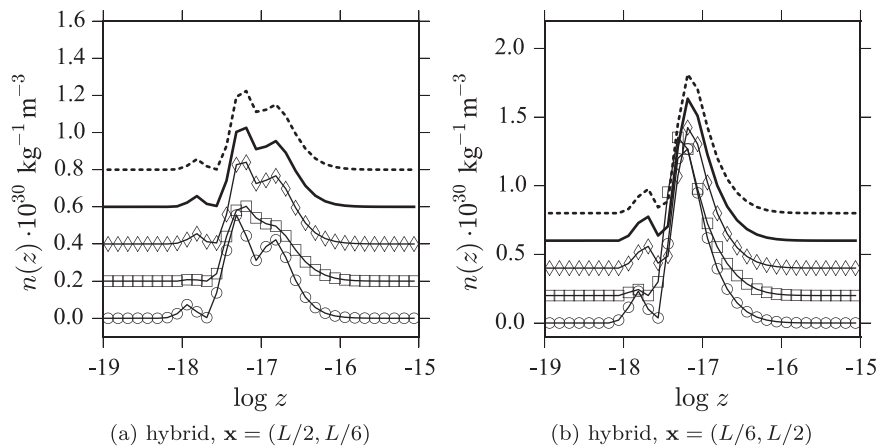


Fig. 8. Droplet size distribution at $t^* = 5$ for $\Delta t = 64 \cdot 10^{-5}$ s (circles), $\Delta t = 32 \cdot 10^{-5}$ s (squares), $\Delta t = 16 \cdot 10^{-5}$ s (diamonds), $\Delta t = 8 \cdot 10^{-5}$ s (solid) and $\Delta t = 4 \cdot 10^{-5}$ s (dotted). Each line in this sequence has a vertical offset of $2 \cdot 10^{29}$ with respect to the previous, for visual clarity. In all figures the grid was 128^2 and $P=8$ sections/decade, while using the hybrid CBSM scheme.

Table 3Convergence of e_{hor} and e_{ver} for a time step size sequence, using $\Delta t = 4 \cdot 10^{-5}$ as reference solution.

$\Delta t \cdot 10^{-5}$	e_{hor}	Order	e_{ver}	Order	max (CFL)
64	0.01641		0.01724		0.96
32	0.00739	1.4897	0.00703	1.5658	0.48
16	0.00294	1.5866	0.00256	1.6559	0.24
8	0.00087	1.8365	0.00067	1.9558	0.12

due to the applied first order upwind scheme in the convective terms. However, the solutions for the 256^2 and 512^2 grids are visually much closer to each other than those for the 32^2 and 64^2 grids, suggesting that the solution converges as the grid is refined. The solution on the 512^2 grid is not yet fully converged though, as features visible in the solution for this grid are not yet visible on the 256^2 grid. As discussed before, it is possible to trade in the upwind scheme for a flux limiter scheme, which would still preserve positivity of the solution. However, this limiter should be ‘global’ with respect to N_i , Z_j and Y_j , yielding one value for each field, in order to preserve constraints (1) and (13). The default schemes available in OpenFOAM do not offer this property. We choose here consistency over accuracy, but acknowledge that for most applications relaxing constraints (1) and (13) by virtue of improving the overall accuracy of the solution may be acceptable too.

Next, the dependence of the solution on the number of sections and the chosen CBSM scheme is studied. Fig. 7 shows for a refinement sequence in P the droplet size distribution, at two positions (corresponding to the dashed lines in Fig. 5b and d), for the two-moment and hybrid CBSM schemes. The distribution is plotted in log z -space, in which the sections have uniform width. Convergence is shown as P increases. The results for the two-moment scheme are generally more diffusive and smoother than the hybrid scheme, for the same P . However, as P increases, small details which are already visible in the hybrid solution also appear in the two-moment result. Both the two-moment and hybrid solution converge towards the same solutions, however, the hybrid one preserves sharp gradients better at lower P . This property was already established in the spatially homogeneous case, see Frederix et al. (2016).

In the modeling of the aerosol size distribution it is common to not fully resolve the distribution, but to work in terms of moments of an assumed distribution. An assumption that is often made is that $\log d$ is normally distributed. Since $\log z$ is proportional to $\log d$, Fig. 7 should, under the log-normal assumption, give a Gaussian bell curve. However, this is clearly not the case, motivating the effort to implement the sectional approach.

The dependence of the solution on the time step size Δt is illustrated in Fig. 8. At two positions the distribution is shown for a sequence of decreasing time step sizes. The dependence of the solution is, for the chosen range of Δt , not as strong as the dependence of the solution on P . A clear convergence is shown, though.

In Section 3 CBSM was integrated within compressible PISO, along with the Crank–Nicolson time discretization scheme, using a fractional step method. This effort was undertaken to retain a second order accurate time integration for the velocity, temperature and pressure solutions. Table 3 shows, for a sequence of Δt refinement, e_{hor} and e_{ver} . The reference solution is taken at $\Delta t = 4 \cdot 10^{-5}$ s. The order of convergence is shown to be smaller than, but close to second order. More importantly, the solution for the perpendicular velocity at the cavity centerlines using $\Delta t = 64 \cdot 10^{-5}$ s is shown to be within 2% of the reference solution, in terms of e_{hor} and e_{ver} .

5. Aerosol nucleation in a double-mixing tee

To illustrate the applicability of the developed method in a 3D complex geometry, in this section we will present simulations of the flow with nucleating aerosol undergoing dynamic evolution in a double-mixing tee chamber. The double-mixing tee is one of the many compartments present in the in vitro exposure system developed by Vitrocell®, which is a subject of ongoing scientific investigations (Adamson et al., 2014; Majeed et al., 2014; Thorne & Adamson, 2013) to characterize its functionality for delivering a controlled dose of substances during in vitro toxicological assessment. In Section 5.1 we give a brief introduction to the geometry, flow conditions and computational grid used for the simulation. Subsequently, in Section 5.2, quantitative predictions of the aerosol that is generated will be discussed. The purpose of these simulations is to demonstrate the suitability of the method without pursuing

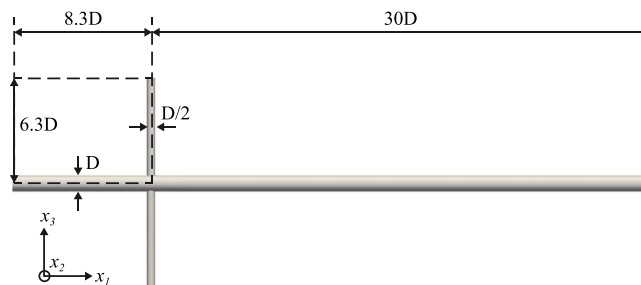


Fig. 9. Computational domain geometry based on the diameter of the main pipe $D = 6$ mm with two dilution legs with the diameter $D/2$.

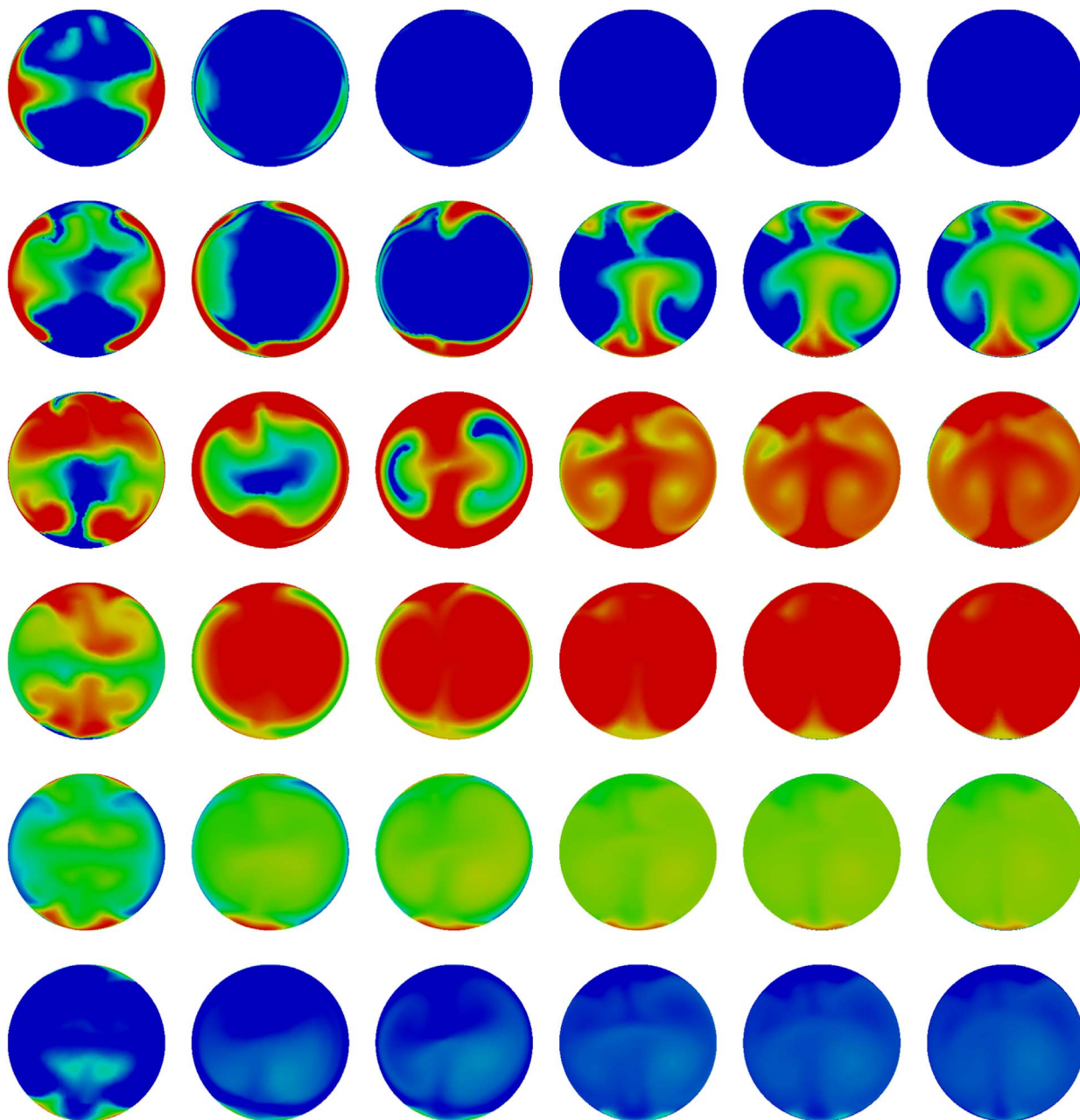


Fig. 10. Instantaneous cross section plots of the droplet number concentration taken at a well-developed flow snapshot ($t = 1$ s). From left to right: $x_1/D = 0.7, 1.7, 2.7, 5.7, 7.7$ and 9.7 downstream of the center of the tee. From top to bottom: particle diameter $d=9$ nm, 31 nm, 50 nm, 80 nm, $0.13 \mu\text{m}$ and $0.21 \mu\text{m}$. The color scale is logarithmic. Red indicates $N = 10^{13} \text{m}^{-3}$ or higher and blue indicates $N = 10^{10} \text{m}^{-3}$ or lower.

high-resolution grid-independence of the results.

5.1. Geometry, mesh and flow conditions

We simulate nucleation from saturated vapors of DBP flowing into the double-mixing tee chamber, which are cooled down by a dilution flow. The choice to work with DBP is made to keep a close connection with the previous section. It is an interesting test situation for the modeling and simulation method, although the relevance of DBP nucleation is largely academic. The geometry used for the simulations together with the dimensions of the system is presented in Fig. 9. The main pipe has a diameter $D = 6$ mm. Two dilution pipes of diameter $D/2$ are attached to the main pipe. In our simulations, the main pipe extends to $8.3 D$ upstream of the junction and $30 D$ downstream and the lengths of the dilution pipes are $6.3 D$ each. These dimensions allow to consider the flow in the central mixing region as quite independent of the inflow and outflow conditions imposed at the various entry and exit points.

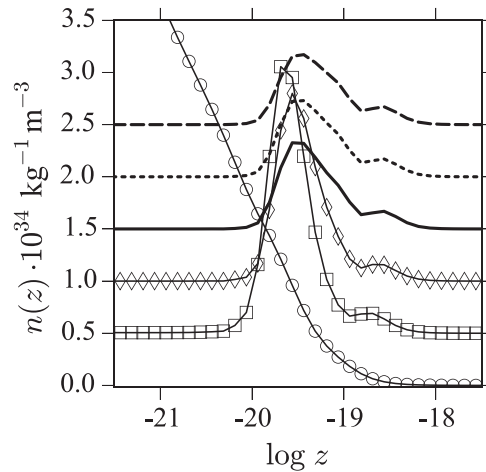


Fig. 11. Instantaneous cross section-averaged droplet size distributions taken at well-developed flow conditions ($t = 1$ s), at $x_1 = 0.7D$ (circles), $1.7D$ (squares), $2.7D$ (diamonds), $5.7D$ (solid), $7.7D$ (dotted) and $9.7D$ (dashed), downstream of the center of the tee. Each distribution is vertically offset by $5 \cdot 10^{33}$.

Flow simulations with coalescing aerosol droplets were performed previously in this geometry (Kuczaj, Nordlund, & Jayaraju, 2016; Kuczaj et al., 2016). The mesh is based on the non-dimensional cell sizes for a flow rate of 12 L/min as reported in Kuczaj, Nordlund, Jayaraju, and Komen (2016). Polyhedral cells are used close to the double-mixing tee region. Further downstream, the mesh elements are extruded in the axial direction on both sides. The total mesh size is about 2.6 million cells and we use it for simulations of a relatively low flow rate of 3 L/min. A typical cross section of the main pipe contains approximately 40^2 – 50^2 cells. This allows to adequately capture the flow structures as emerge in the central mixing region. It was shown in Kuczaj, Nordlund, Jayaraju, and Komen (2016) that the resolution is sufficient to capture the expected unsteady flow in the mixing chamber. For more details regarding the mesh the reader is referred to Kuczaj, Nordlund, Jayaraju, and Komen (2016). The time step is restricted by the CFL condition, where the max CFL number is allowed to be 0.75.

The saturated DBP vapor inflow rate (carrying both saturated vapor and air) for typical test conditions is 1.5 L/min and the dilution flow is 0.75 L/min per mixing-tee leg. This gives in total 3 L/min downstream of the mixing chamber, a bulk Reynolds number $Re=636$ based on the main pipe diameter and an average flow-through time of approximately 0.1 s. Parabolic velocity profiles and zero-gradient pressure conditions were applied to all inlets and a fixed atmospheric pressure boundary condition is imposed at the outlet. The hot DBP vapors entering the system at temperature T_0 are cooled down by the two dilution flows, both at temperature T_∞ . T_0 and T_∞ take the same values as used in Section 4, i.e., $T_0=373.15$ K and $T_\infty = 273.15$ K. Also in agreement with Section 4, at the main inlet we set a uniform perfect saturation condition for the DBP vapor mass fraction: $Y = Y_{DBP}^s(T_0)$ at the inlet (again, physicochemical properties are taken from Frederix et al., 2015). Adiabatic conditions are applied on all geometry walls.

The previous section suggests that for these conditions, when using the hybrid CBSM scheme, a reliable sectional solution is obtained at 8 sections/decade, see for example Fig. 7. We use this value for the number of sections in the double-mixing tee simulations.

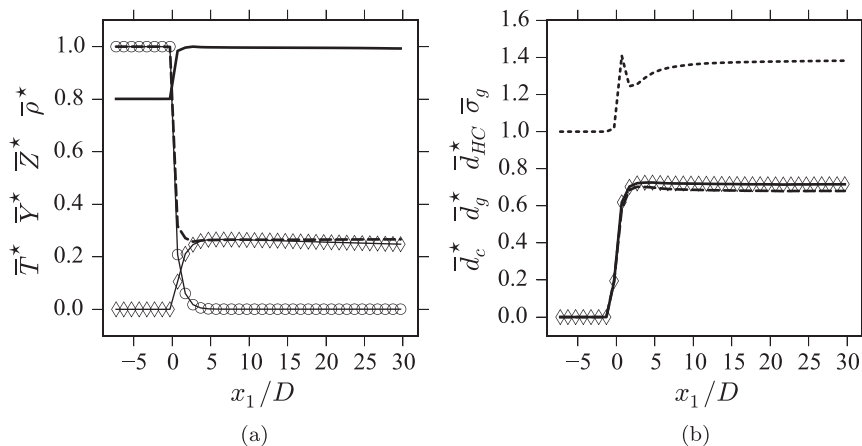


Fig. 12. (a) The non-dimensional temperature \bar{T}^* (dashed), density $\bar{\rho}^*$ (solid), DBP vapor mass fraction \bar{Y}^* (circles), and DBP liquid mass fraction \bar{Z}^* (diamonds). (b) The count mean diameter $\bar{d}_c^* = \bar{d}_c/10^{-7}$ (solid), geometric mean diameter $\bar{d}_g^* = \bar{d}_g/10^{-7}$ (dashed), theoretical count mean diameter $\bar{d}_{HC}^* = \bar{d}_{HC}/10^{-7}$ (diamonds) and geometric standard deviation $\bar{\sigma}_g$ (dotted). All curves are as a function of the scaled horizontal coordinate where $x_1 = 0$ m is the center of the tee.

5.2. Aerosol flow results

Localized mixing of the hot saturated DBP vapor flow with the cold air flow triggers nucleation of the aerosol together with its further immediate growth by condensation, which is captured by the sectional method. The dilution flow generates a shear layer while entering the main pipe flow, causing flow instability and shedding of vortical flow structures that laminarize further downstream at the selected flow Reynolds number. This was shown in [Kuczaj, Nordlund, Jayaraju, and Komen \(2016\)](#). The vapor flow is abruptly cooled by the convective supply of cold air, leading to very sharp temperature gradients in the mixing chamber. Aerosol is generated in close proximity to the shear layer. [Fig. 10](#) shows, for six droplet sizes, the instantaneous droplet number concentrations at six consecutively placed cross sections of the pipe downstream of the mixing chamber. In this snapshot, the formation of aerosol is clearly asymmetric in space, due to the unsteady behavior of the flow. It can be seen that several flow structures are formed. These structures are, by visual inspection, not smaller than $D/5$. We expect that the formed aerosol is captured reliably on our computational mesh with 4 to 5 grid cells available for the smallest scales in the solution. [Fig. 10](#) shows that close to the mixing chamber there are many small droplets. At larger distances the small droplets have grown to larger sizes due to condensation. Droplets of sizes around $d=80$ nm are present most significantly. For larger distances from the mixing chamber the concentration plots appear to become more uniform. Visually comparing cross sections five and six (at distances $7.7D$ and $9.7D$), we conclude that around this distance the evolution of the aerosol has ceased.

In [Fig. 11](#), the cross section-averaged size distribution is shown. Clearly, close to the mixing chamber many small droplets exist. The shape of the distribution is significantly different in comparison to later cross sections, due to nucleation. For larger distances it is shown that a relatively narrow distribution is formed which, for even larger distances, grows into a weakly bi-modal wider distribution.

In [Fig. 12](#) cross section-averaged quantities that depict the behavior of the flow and aerosol in the main pipe geometry are presented. In the remainder, we denote cross section-averaging by an overline. The scaled (indicated by *) and cross section-averaged vapor mass fraction \bar{Y}^* nucleates and subsequently condenses near $x=0$ m turning into the scaled liquid mass fraction \bar{Z}^* . This process is driven by a significant drop of the temperature, \bar{T}^* , caused by the cold dilution flow. Because of the cold incoming dilution flow the density $\bar{\rho}^*$ (scaled by the steady state solution ρ_∞) increases and the partitioning between vapor and air mass fractions is affected. Without dilution, the downstream value of \bar{Z}^* would become the upstream value of \bar{Y}^* , i.e., all vapors are turned into liquid, both having the same concentration. This was the case in the cavity, see for example [Fig. 4](#). With dilution, the liquid concentration is reduced, as shown in the solution for \bar{Z}^* .

In [Fig. 12](#) a number of statistical mixture quantities are presented (in red). First, the cross section-averaged count mean diameter \bar{d}_c is shown, directly computed from the sectional simulation data, as ([Hinds, 1999](#)):

$$d_c = \frac{\sum_i N_i d_i}{N}, \quad (32)$$

with d_i being the diameter of a droplet in section i and $N = \sum_i N_i$. If no droplets are present on the cross section surface, \bar{d}_c is set to zero. [Fig. 12](#) shows, as expected, an increase in \bar{d}_c as a function of downstream position. The droplet size is one order of magnitude smaller than that reported in case of the laminar flow diffusion chamber ([Nguyen et al., 1987](#)), as well as in the cavity, because of cooling of saturated vapors by the high dilution flow rather than mainly diffusive cooling. In this case, more rapid cooling leads to a larger number of droplets at smaller sizes.

The cross section-averaged geometric standard deviation $\bar{\sigma}_g$ is shown, also directly computed from the simulation data, using

$$\ln \sigma_g = \sqrt{\frac{\sum_i N_i (\ln d_i - \ln d_g)^2}{N}}, \quad (33)$$

and where d_g is the geometric mean diameter, given by

$$\ln d_g = \frac{\sum_i N_i \ln d_i}{N}, \quad (34)$$

of which its cross section-average \bar{d}_g is also shown in [Fig. 12](#). In the case of a log-normal size distribution, a common assumption to reduce the complexity of the aerosol model, the geometric mean diameter d_g equals the count median diameter CMD. In that case we can use the so-called Hatch–Choate conversion equations ([Hinds, 1999](#)) to compute d_c from d_g and σ_g :

$$d_{HC} = \text{CMD} \exp\left(\frac{1}{2} \ln^2 \sigma_g\right), \quad (35)$$

where d_{HC} becomes the ‘theoretical’ count mean diameter. The level of agreement between this theoretical prediction and the value obtained from the full simulation is a measure for the log-normality of the distribution. [Fig. 12](#) shows that both cross section-averaged quantities are close to each other with a relative deviation less than 1%, suggesting log-normality. After inspection of the actual cross-section averaged distributions in [Fig. 11](#) we conclude that for distances away from the nucleation zone the log-normal assumption appears quite effective (distributions are rather symmetrical in $\log z$ -space). However, within the nucleation zone in the center of the mixing tee the log-normal distribution is clearly invalid because there is a preference for smaller droplet sizes. This motivates the use of the sectional method, in order to capture nucleation accurately and hence also predict correct sizes of the aerosol further downstream.

The cross section-averaged geometric standard deviation σ_g remains well below 1.5, suggesting that over the plane of averaging

droplets are rather mono-disperse. Close to the nucleation zone, around $x_1/D = 0$, the geometric standard deviation is largest, due to the presence of both freshly nucleated droplets as well as already condensed droplets. This example illustrates that CBSM is capable of efficiently resolving both sizes.

6. Conclusions

In this paper we adapted the CBSM method to the complete set of fluid equations of motion for a compressible flow formulation with a dispersed aerosol liquid phase. By using the fractional step method, spatial terms could be isolated from the ‘internal’ terms such as those describing coalescence, condensational growth and nucleation. This allowed for the introduction of CBSM to solve the spatially homogeneous size distribution equation, embedded in a spatially heterogeneous setting.

First, the method was applied to the modeling of aerosol formation in a lid-driven cavity. The accuracy of the method, the control we have over the truncation error and the influence of two different CBSM schemes (two-moment-preserving and hybrid) were studied by means of a grid refinement sequence, in terms of spatial, temporal and sectional resolution. The dependence of the solution on the chosen grid resolution is, for the cavity, large, given that all convective terms are treated using the first order upwind scheme. However, convergence of the solution is shown. We also measured a convergence of the solution for a sectional refinement sequence, for both CBSM distribution schemes. The hybrid scheme, reducing from four-moment to two-moment-preservation to avoid negativity, as was shown in Frederix et al. (2016), gives at coarse (i.e., 8 sections per decade) sectional distributions already sharp results. Finally, we showed that the accuracy of the time integration of the velocity and pressure remains as desired; a simulation with a CFL number of unity is shown to be within 2% of a simulation with a 16 times smaller time step size.

The cavity simulations demonstrated the feasibility of the extension of the CBSM method to spatially heterogeneous settings, yet still in two spatial dimensions. To illustrate the feasibility and applicability of the developed method further, we applied it to the simulation of aerosol formation in a double mixing-tee. The CBSM provided detailed information regarding the unsteady and spatially varying formed aerosol size distributions. It was shown that in the double mixing-tee the size distribution grows to a distribution which could be effectively modeled as a log-normal distribution. However, within the nucleation zone, the droplet size distribution is far from log-normal, motivating the choice for a sectional method.

Acknowledgments

The research presented in this work was funded by Philip Morris Products S.A. (part of Philip Morris International group of companies).

References

- Adamson, J., Thorne, D., Errington, G., Fields, W., Li, X., Payne, R. et al. (2014). An inter-machine comparison of tobacco smoke particle deposition in vitro from six independent smoke exposure systems. *Toxicology in Vitro*, 7, 1320–1328.
- Erturk, E., Corke, T. C., & Gökçöl, C. (2005). Numerical solutions of 2-D steady incompressible driven cavity flow at high Reynolds numbers. *International Journal for Numerical Methods in Fluids*, 48(7), 747–774.
- Frederix, E. M. A., Stanic, M., Kuczaj, A. K., Nordlund, M., & Geurts, B. J. (2016). Characteristics-based sectional modeling of aerosol nucleation and condensation. *Journal of Computational Physics*, 326, 499–515.
- Frederix, E. M. A., Stanic, M., Kuczaj, A. K., Nordlund, M., & Geurts, B. J. (2015). Extension of the compressible PISO algorithm to single-species aerosol formation and transport. *International Journal of Multiphase Flow*, 74, 184–194.
- Friedlander, S. K. (2000). *Smoke, dust, and haze: Fundamentals of aerosol dynamics* (2nd edition). Oxford University Press ISBN: 0471014680.
- Gelbard, F., Tambour, Y., & Seinfeld, J. H. (1980). Sectional representations for simulating aerosol dynamics. *Journal of Colloid and Interface Science*, 76(2), 541–556.
- Ghia, U., Ghia, K. N., & Shin, C. T. (1982). High-Re solutions for incompressible flow using the Navier–Stokes equations and a multigrid method. *Journal of Computational Physics*, 48(3), 387–411.
- Giovangigli, V. (1991). Convergent iterative methods for multicomponent diffusion. *IMPACT of Computing in Science and Engineering*, 3(3), 244–276.
- Hinds, W. C. (1999). *Aerosol technology* (2nd edition). John Wiley & Sons, Inc. ISBN: 0471194107.
- Issa, R. I., Ahmadi-Befruj, B., Beshay, K. R., & Gosman, A. D. (1991). Solution of the implicitly discretised reacting flow equations by operator-splitting. *Journal of Computational Physics*, 93(2), 388–410.
- Issa, R. I. (1986). Solution of the implicitly discretised fluid flow equations by operator-splitting. *Journal of Computational Physics*, 62(1), 40–65.
- Kuczaj, A. K., Nordlund, M., Jayaraju, S., & Komen E., (2016). Flow characterization in a double-tee junction dilution unit of exposure system, in preparation.
- Kuczaj, A. K., Nordlund, M., Jayaraju, S., Komen, E., Krebs, T., Peitsch, M., et al. (2016). Aerosol flow in the Vitrocell® 24/48 exposure system: Flow mixing and aerosol coalescence. *Applied In Vitro Toxicology*, submitted for publication, <http://online.liebertpub.com/doi/abs/10.1089/aivt.2016.0009>.
- Kumar, S., & Ramkrishna, D. (1996). On the solution of population balance equations by discretization-I. A fixed pivot technique. *Chemical Engineering Science*, 51(8), 1311–1332.
- Lee, K. W., & Chen, H. (1984). Coagulation rate of polydisperse particles. *Aerosol Science and Technology*, 3(3), 327–334.
- Majeed, S., Frentzel, S., Wagner, S., Kuehn, D., Leroy, P., Guy, P. A. et al. (2014). Characterization of the Vitrocell® 24/48 in vitro aerosol exposure system using mainstream cigarette smoke. *Chemistry Central Journal*, 8(62).
- Morton, K. W., & Mayers, D. F. (2005). *Numerical solution of partial differential equations*. Cambridge University Press ISBN: 0521607930.
- Nguyen, H. V., Okuyama, K., Mimura, T., Kousaka, Y., Flagan, R. C., & Seinfeld, J. H. (1987). Homogeneous and heterogeneous nucleation in a laminar flow aerosol generator. *Journal of Colloid and Interface Science*, 119(2), 491–504.
- Ramkrishna, D. (2000). *Population balances theory and applications to particulate systems in engineering*. Academic Press ISBN: 0123911486.
- Thorne, D., & Adamson, J. (2013). A review of in vitro cigarette smoke exposure systems. *Experimental and Toxicologic Pathology*, 65, 1183–1193.
- Walas, S. M. (1985). *Phase equilibria in chemical engineering*. Butterworth-Heinemann ISBN: 0409951625.
- Wilck, M., & Stratmann, F. (1997). A 2-D multicomponent modal aerosol model and its application to laminar flow reactors. *Journal of Aerosol Science*, 28(6), 959–972.
- Winkelmann, C., Kuczaj, A. K., Nordlund, M., & Geurts, B. J. (2016). Simulation of aerosol formation due to rapid cooling of multispecies vapors. *Journal of Engineering Mathematics*, submitted for publication.